Expert Systems With Applications 180 (2021) 115012

Contents lists available at ScienceDirect

Expert Systems With Applications

journal homepage: www.elsevier.com/locate/eswa

Dynamic few-view X-ray imaging for inspection of CAD-based objects

Alice Presenti *, Jan Sijbers, Jan De Beenhouwer

imec-VisionLab, Dept. of Physics, University of Antwerp (CDE), Universiteitsplein 1, Building N, B-2610 Antwerp, Belgium

ARTICLE INFO

Keywords:
Few-view inspection
CAD
Dynamic acquisition
Visibility angles
Pose estimation

ABSTRACT

X-ray 3D Computed Tomography (3DCT) has great potential for inspection of industrial products. Unfortunately, conventional CT-based workflows to inspect objects created from a CAD model involve a time-consuming acquisition process, computationally expensive image reconstruction, and multiple postprocessing steps, preventing them from inline usage. In this paper, we propose DynaPose, a fast and yet accurate workflow for 3D X-ray inspection of objects created from a CAD model. By exploiting prior knowledge of the CAD model, and relying on only very few radiographs, inspection can be performed in real-time. The DynaPose method allows automated 3D pose estimation of the object to be inspected while dynamically acquiring radiographs that are optimal for the detection task. Through simulation and real experiments, we show that our approach paves the way for inline inspection of manufactured objects.

1. Introduction

In recent years, the manufacturing industry has become increasingly interested in X-ray 3D Computed Tomography (3DCT) as an inline inspection method. This non-destructive technique allows the reconstruction of a 3D image from a set of radiographs acquired at different angular views. For inspection of manufactured objects, the reconstructed 3DCT volume is, then, compared with the nominal geometry and composition, provided, for example, by a computer-aided design (CAD) model.

Conventional 3DCT inspection is a multistep procedure. From a large set of acquired radiographs, a 3D image is reconstructed and subsequently segmented. Next, a polygon-based isosurface is extracted for alignment with the reference CAD model. Finally, the two surfaces are compared to quantify deviations from the nominal geometry (Kruth et al., 2011; Kiekens et al., 2011; Brunke, 2012; Noel, 2008).

This procedure, however, suffers from multiple limitations. First of all, conventional 3DCT requires hundreds to thousands of radiographs to enable the reconstruction of a high-quality volumetric image, which is time-consuming and hence impractical for fast inline scanning. Secondly, to prevent artifacts in the reconstructed 3D image, a full angular range acquisition is needed, which may not be possible in inline settings. Finally, the reconstructed 3DCT images may be affected by artifacts (caused by, for example, beam hardening, misalignments, noise or scatter Hiller & Hornberger, 2016), which hinder posterior segmentation and polygon mesh extraction and introduce errors that propagate to the quantification step.

Many attempts to reduce the reconstruction artifacts were addressed in the literature. For example, Zhang et al. (2016) proposed a deep convolutional neural network to suppress artifacts in FBP reconstructions generated from limited angle data. By mapping the reconstruction to artifact-free reconstructions, features describing artifacts were extracted and reduced by nonlinear mapping, and a corrected image was produced as output. The problem of sparse view acquisition was also addressed by Purisha, Jidling, Wahlström, Särkkä, and Schön (2018). In their paper, a Gaussian model was used to reconstruct the measured object from only nine projections. However, suppressing the artifacts introduced a strong blurring to the resulting images. Moreover, the computation time on a single phantom was high (more than 2 h), making this method not suitable for real-time inspection.

As an alternative to conventional 3DCT based inspection, object features can be directly estimated from a limited number of acquired radiographs and compared to the nominal geometry. Compared to 3DCT techniques, projection-based inspection has multiple advantages. Indeed, by skipping the 3D reconstruction, segmentation, and Standard Triangle Language (STL) extraction steps, various sources of errors that could influence the effectiveness of the final inspection are excluded. By performing inspection directly on the radiographs, a volumetric reconstruction can be avoided and the number of acquired radiographs (and hence acquisition time) can be reduced by two orders of magnitude. Few studies have been published on radiograph-based inspection. For example, Yin, Khare, and De Man (2009) and Haario et al. (2016)

* Corresponding author.
E-mail addresses: alice.presenti@uantwerpen.be (A. Presenti), jan.sijbers@uantwerpen.be (J. Sijbers), jan.debeenhouwer@uantwerpen.be (J. De Beenhouwer).

https://doi.org/10.1016/j.eswa.2021.115012
Received 8 June 2020; Received in revised form 16 January 2021; Accepted 7 April 2021
Available online 20 April 2021

estimated the object's boundary parameters from a small number of 2D parallel beam radiographs, assuming the object to consist of a single material. Noble et al. (1995) performed calibration of a drilling plan by recovering the 3D coordinates of points appearing in multiple radiographs and registering these coordinates with those of the CAD model. This, however, required fiducial markers to be present in the object and the corresponding CAD coordinates to be known. Carrasco and Mery (2011) performed automatic inspection by geometrically combining features appearing in different images. In their paper, flaws were identified and tracked if they appeared in a sequence of multiple radiographs. Multi-view detection and tracking was used by Mery (2015) to detect parts from complex objects with 95.7% precision and 93.9% recall, and for object recognition with an accuracy of 96.5%. In Valavanis and Kosmopoulos (2010), defects in weld radiographs are detected and classified based on texture and geometrical features. Based on real data experiments, three classification methods (multi-class Support Vector Machine (SVM), Artificial Neural Network (ANN) and k nearest neighbor (k-NN)) were compared: ANN and SVM classifier reached both around 85% accuracy, while the k-NN approach returned significantly lower results. A similar approach was adopted in Zapata, Vilar, and Ruiz (2011) to detect four weld defects and non-defect objects. The accuracy was 78.9% for the ANN and 82.6% for the ANFIS. However, both methods lack 3D spatial information and are limited to the detection of cracks or holes. Mery and Arteta (2017) compared 24 techniques to identify flaws on projections. In their tests, the best performance was achieved by a local binary pattern (LBP) descriptor with an SVM-linear classifier, obtaining 95.2% of accuracy. Hou, Wei, Guo, Jin, and Zhu (2018) performed automatic detection of welding defects by using a neural network trained on small regions of interest for binary classification (defective/intact). A sliding window technique was then applied to inspect the images. Similarly, Boaretto and Centeno (2017) identified welding defects by using neural networks. In their paper, a network was used to classify into five different categories corresponding to four different defects and non-defective products. This network reached an accuracy of 79.5%. Better accuracy of 88.6% was obtained, instead, with a binary classifier.

An intrinsic weakness of radiograph-based analysis is the lack of 3D spatial localization. Possible defects are assumed to be visible from every angle or require that the object pose is known beforehand. To solve these issues, we propose DynaPose, a dynamic acquisition strategy that allows fast radiograph-based 3D inspection of manufactured objects. When inspecting manufactured products, it is usually well-known which are the most common defects, for example resulting from the assembly of components. Based on an a priori-defined region of interest for inspection, a strategy is proposed to optimally detect possible flaws from a limited, task-specific set of radiographs, determined by exploiting prior knowledge of the object's CAD model based on simulated data. Such an approach is particularly relevant when a set of recurrent defects can be identified. By exploiting the information on the acquisition geometry and the object shape, no prior knowledge of the pose of the object in the X-ray system is needed, as it can be iteratively estimated directly from projection data and improved during the acquisition. To make real-time inspection feasible, based on the estimated object pose, the system is driven towards the acquisition of only the pre-determined set of radiographs. Compared to state of the art methods, our strategy enables the comparison between the measured object and its reference model directly in the projection space. By skipping the reconstruction, it paves the way towards real-time, few-view and limited angle inspection of manufactured objects. We demonstrate the effectiveness of DynaPose on simulated and real data of assembled, complex objects.

2. Methods

In this section, we first define the acquisition system geometry and describe the assumptions made about the object pose in Section 2.1. Radiograph-based inspection relies on comparing measured with simulated radiographs. Therefore, realistic radiograph simulation from CAD models is described in Section 2.2. Subsequently, in Section 2.3, we outline a method to determine a limited set of radiographs tailored to a specific inspection task. To dynamically compare simulated with acquired radiographs, accurate and fast pose estimation is key. We propose a structured library approach based on pre-calculated radiographs. Details on the creation of structured radiograph libraries are given in Section 2.4. Finally, in Section 2.5, the procedure to dynamically acquire the pre-determined set of radiographs is described.

2.1. The system geometry

In what follows, we will assume a circular cone beam acquisition geometry, with the source and detector pair rotating around a fixed object. The method can, however, easily be adapted to other acquisition geometries.

Let $\mathscr{S} = \{\mathbf{x}, \mathbf{y}, \mathbf{z}\}$ be a reference system, with the $\mathbf{y}$ and $\mathbf{z}$ axis parallel to the detector plane, and $\mathbf{x}$ directed along the initial source-detector line. The barycenter of the CAD model coincides with the center $\mathbf{O} = (0, 0, 0)$ of $\mathscr{S}$. The orientation and position of the object in the acquisition system define a new coordinate system $\mathscr{S}_{RT} = \{\mathbf{x}_{RT}, \mathbf{y}_{RT}, \mathbf{z}_{RT}\}$ centered in $\mathbf{O_{RT}} = \{t_x, t_y, t_z\}$, the barycenter of the object (see Fig. 1a). The orientation of the object with respect to $\mathscr{S}$ is uniquely defined by the rotation angles φ, δ and γ around $\mathbf{x}, \mathbf{z}'$ and $\mathbf{y}''$, respectively, with $\mathbf{z}' = \mathbf{R_x}(\varphi)\mathbf{z}$ and $\mathbf{y}'' = \mathbf{R_{z'}}(\delta)\mathbf{R_x}(\varphi)\mathbf{y}$ (see Fig. 1b), where $\mathbf{R_u}(\theta)$ is the matrix describing the rotation by an angle θ around the axis $\mathbf{u} = (u_x, u_y, u_z)$:

$$\mathbf{R_u}(\theta) = \begin{pmatrix} \cos\theta + u_x^2(1-\cos\theta) & u_x u_y(1-\cos\theta) - u_z\sin\theta & u_x u_z(1-\cos\theta) + u_y\sin\theta & 0 \\ u_y u_x(1-\cos\theta) + u_z\sin\theta & \cos\theta + u_y^2(1-\cos\theta) & u_y u_z(1-\cos\theta) - u_x\sin\theta & 0 \\ u_z u_x(1-\cos\theta) - u_y\sin\theta & u_z u_y(1-\cos\theta) + u_x\sin\theta & \cos\theta + u_z^2(1-\cos\theta) & 0 \\ 0 & 0 & 0 & 1 \end{pmatrix}. \tag{1}$$

The translation matrix that transforms $\mathbf{O}$ in $\mathbf{O_{RT}}$ is defined by

$$\mathbf{T} = \begin{pmatrix} 1 & 0 & 0 & 0 \\ 0 & 1 & 0 & 0 \\ 0 & 0 & 1 & 0 \\ t_x & t_y & t_z & 1 \end{pmatrix}. \tag{2}$$

Thus, the transformations that map $\mathbf{x}, \mathbf{y}, \mathbf{z}$ to $\mathbf{x}_{RT}, \mathbf{y}_{RT}, \mathbf{z}_{RT}$ are given by

$$\begin{aligned} \mathbf{x_{RT}} &= \mathbf{R_{y''}}(\gamma)\mathbf{R_{z'}}(\delta)\mathbf{x} + \mathbf{T}, \\ \mathbf{y_{RT}} &= \mathbf{R_{z'}}(\delta)\mathbf{R_x}(\varphi)\mathbf{y} + \mathbf{T}, \\ \mathbf{z_{RT}} &= \mathbf{R_{y''}}(\gamma)\mathbf{R_x}(\varphi)\mathbf{z} + \mathbf{T}. \end{aligned} \tag{3}$$

Both the position and the orientation of the object are unknown with respect to the reference system $\mathscr{S}$. In many industrial inspection tasks, however, assumptions can be made about the pose of the object to be inspected. In our paper, we assume that the sample is placed approximately straight into a holder. That is, only the rotation around the vertical axis is considered unconstrained ($\gamma \in [0, 360)^\circ$), while δ and φ are assumed to vary within narrower intervals $[\delta_{\min}, \delta_{\max}]$, $[\varphi_{\min}, \varphi_{\max}]$, respectively.

2.2. Realistic simulation of radiographs from a CAD model

For fast simulation of radiographs from a CAD model, we rely on an in–house developed CAD projector introduced by Marinovszki, De Beenhouwer, and Sijbers (2018). In this projector, the intersection length of each virtually casted ray crossing the CAD model is calculated and, knowing the absorption coefficient μ_m of material m, polychromatic radiographs are created based on the discrete polychromatic form of the Beer–Lambert law:

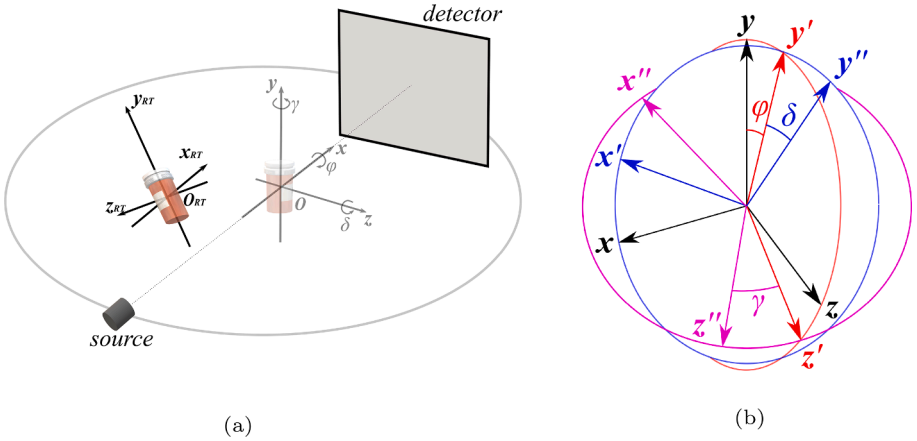

Fig. 1. The system's geometry (a) and of the Euler angles γ, δ and φ (b).

$$I_r = \sum_{i=1}^{n} W(E_i) e^{-\sum_m \mu_m(E_i) l_{r,m}} \Delta E_i \tag{4}$$

where I_r is the r-th pixel intensity, and $l_{r,m}$ is the geometric distance that the ray travels from the source to the r-th pixel through material m. The energy spectrum of the source is subdivided in n energy bins ΔE_i, and $W(E_i)$ is the weight of the i-th bin.

For an accurate simulation of radiographs, knowledge of the source spectrum $\{W(E_i), i = 1, \ldots, n\}$ is required. The source spectrum is estimated with a radiograph-based method, by minimizing the discrepancy between the intensity values of measured and simulated data with respect to the energy bin weights, as in Six, De Beenhouwer, and Sijbers (2019).

2.3. Visibility angles

In this section, a set of projection angles that are optimal in terms of a chosen contrast criterion are determined through simulated projections using the object's CAD model. During inspection of the object, these projections will then be acquired based on the simultaneous dynamic estimation of the object pose. Let $f(\gamma)$ be the function describing a task-dependent criterion that needs to be optimized in terms of the object's orientation. In our work, $f(\gamma)$ is the visibility of a component compared to its surrounding background. Suppose we want to acquire K radiographs. We define $\Omega = \{\gamma_{vis}^1, \ldots, \gamma_{vis}^K\}$ as the ordered set of the *visibility angles* that optimize $f(\gamma)$, where the γ_{vis}^k are obtained with a greedy algorithm:

Algorithm 1: Greedy algorithm to define the visibility angles

$\Gamma_1 = [0, 360)$;
for $k = 1, \ldots, K$ **do**
  $\gamma_{vis}^k = \arg\max_{\gamma \in \Gamma_k} f(\gamma)$;
  $\Gamma_{k+1} = \Gamma_k \setminus [\gamma_{vis}^k - \alpha, \gamma_{vis}^k + \alpha]$;
end

In Algorithm 1, α is a user-defined minimum angular distance to prevent acquiring radiographs close to already acquired projections.

In our experiments, we chose a contrast-based criterion to select those (simulated) radiographs for which the visibility of a certain CAD model component is highest, where the *visibility contrast* is defined as:

$$f(\gamma) = \frac{I(\gamma)_{\max} - I(\gamma)_{\min}}{I(\gamma)_{\max} + I(\gamma)_{\min}}, \tag{5}$$

where $I(\gamma)$ is the simulated projection at orientation γ, and $I(\gamma)_{\max}$ and $I(\gamma)_{\min}$ are its maximum and minimum intensities, respectively. We calculated the contrast only within the border region of the component to be inspected.

2.4. Pre-calculated libraries of simulated radiographs

To detect possible deviations of the sample from the nominal geometry, a fast 2D/3D alignment is crucial. Most alignment methods require an optimization method, which is computationally too intensive for real-time applications (e.g. at production speed). For this reason, we opted for pre-computed libraries of simulated radiographs to be used during the inspection and alignment process.

The barycenter of the CAD model coincides, by definition, with the origin of the reference system $\mathscr{S}$. The object's pose parameters are, instead, expected to vary for every sample. To estimate the pose of the object, its acquired projections are aligned to simulated library images of the CAD model at different orientations. By joining the information on orientation obtained from the 2D comparison at different views, the 3D orientation of the object can be retrieved (the methodology will be described in Section 2.5). A library of simulated radiographs (referred to as *γ-library*) is generated with the calibrated rotation axis parameters and the estimated source spectrum as input, while rotating the object around its rotation axis by $\gamma \in [0, 360)$ at discretized, equiangular steps. In order to account for the deviation of φ and δ and improve the pose estimation, *extended libraries* are generated at the vicinity of the visibility angles. The k-th extended library, for $k = 1, \ldots, K$, is built by discretely varying $\varphi \in [\varphi_{\min}, \varphi_{\max}], \delta \in [\delta_{\min}, \delta_{\max}]$ and $\gamma \in [\gamma_{vis}^k - \epsilon, \gamma_{vis}^k + \epsilon]$. We determined the interval range ϵ from the highest absolute error on the estimate of γ, obtained from the comparison between the γ-library and simulated images with the rotation parameters in their range of definition. To reduce memory requirements, the libraries can be restricted to regions of interest (ROIs) enclosing the object parts to be inspected. The ROIs must be selected for the alignment method to work properly. For example, in our experiments, the ROIs included parts of the outer contour of the object, a feature that may help the image registration algorithm not to converge to the wrong estimates.

2.5. Dynamic radiographs acquisition

When the object is placed in the scanner, its orientation γ, δ and φ and translation t_x, t_y and t_z from the center $\mathbf{O}$ of the reference system $\mathscr{S}$ is unknown. In order to acquire successive radiographs from angles as close as possible to the visibility angles, the object's pose has to be

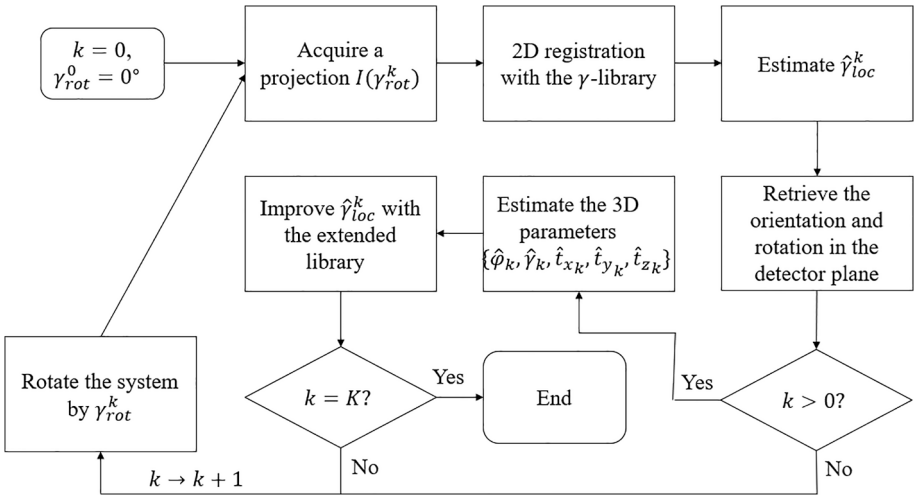

Fig. 2. A schematic overview of DynaPose.

estimated. A schematic flowchart of the procedure is shown in Fig. 2.

Let $\mathbf{S}_k$ be the source position, $\mathbf{D}_k$ the detector center, γ^k_{rot} the source-detector pair rotation angle around $\mathbf{y}$, $\mathbf{u}_k$ and $\mathbf{v}_k$ the unit vectors parallel to the detector edges at iteration k ($\mathbf{u}_0 = (0,1,0), \mathbf{v}_0 = (0,0,1)$). We assume $\mathbf{S}_0$ and $\mathbf{D}_0$ to be known after calibration and $\gamma^k_{rot} = 0$. To retrieve the orientation and position of the sample while dynamically acquiring projections at the visibility angles, the following procedure is followedfrom $k = 0$:

1. A radiograph $I(\gamma^k_{rot})$ is acquired at the current system orientation γ^k_{rot}.
2. The γ-library images are aligned to the measured projection $I(\gamma^k_{rot})$, based on a similarity transformation (i.e. consisting of translation, rotation and scale), with mutual information as a registration criterion.
3. After alignment, the structural similarity (SSIM) index between the measured projection and the images in the γ-library is calculated, and the orientation of the object γ^k_{loc} is retrieved as follows:
   (a) If $k = 0$, $\hat{\gamma}^k_{loc}$ is set to the value corresponding to the highest SSIM.
   (b) If $k > 0$, $\hat{\gamma}^k_{loc}$ is set to the angle corresponding to the local maximum of SSIM closest to γ^k_{vis}.
   (c) The similarity matrix $\mathbf{S}$ between $I(\gamma^k_{rot})$ and $I(\gamma^k_{loc})$ (the library image corresponding to γ^k_{loc}):

$$\mathbf{S} = \begin{pmatrix} \beta\cos\rho & -\beta\sin\rho & 0 \\ \beta\sin\rho & \beta\cos\rho & 0 \\ t^{det}_z & t^{det}_y & 1 \end{pmatrix} \tag{6}$$

describes the translations t^{det}_z and t^{det}_y, the rotation angle ρ and the scaling factor β between the radiographs in the detector plane. The origin of the matrix $\mathbf{S}$ is the projection of $\mathbf{O}$ on the detector, thus,

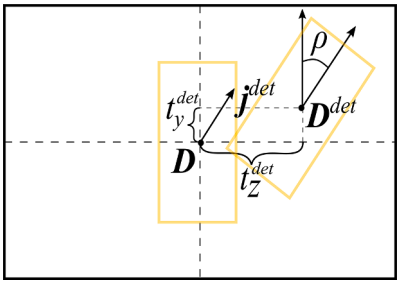

Fig. 3. Scheme of the geometry in the detector plane.

from the 2D parameters t^{det}_z, t^{det}_y and ρ, the 3D orientation of the object can be estimated.

4. The object's orientation and translation in the detector plane are defined by the unit vectors $\mathbf{j}^{det}_k = \mathbf{D}_k + \cos\rho\mathbf{u}_k + \sin\rho\mathbf{v}_k$ and $\mathbf{D}^{det}_k = \mathbf{D}_k + t^{det}_y\mathbf{u}_k + t^{det}_z\mathbf{v}_k$, respectively (see Fig. 3).
5. If $k > 0$, the 3D parameters are estimated fromthe calculated 2D transformations at all previously acquired projections (see Fig. 4):
   (a) Let l_i be the line through $\mathbf{S}_i$ and $\mathbf{D}^{det}_i$, for $i = 0, \ldots, k$. The barycenter of the object, $\mathbf{O}_{RT}$, is estimated as the point $\widehat{\mathbf{O}}^{RT}_k$ that minimizes the distance between the lines $l_0, \ldots, l_k$ (Eikenes, 2020). Its coordinates are the estimates $\hat{t}_{x_k}, \hat{t}_{y_k}$ and $\hat{t}_{z_k}$.
   (b) Let m_i be the line through $\mathbf{S}_i$ and $\mathbf{j}^{det}_i$, for $i = 0, \ldots, k$. To recover the 3D orientation of the object, the point $\widehat{\mathbf{P}}_k$, that minimizes the distance between the lines $m_0, \ldots, m_k$, is calculated. Thus,

$$\mathbf{j}'_k = \frac{\overrightarrow{\mathbf{O}\widehat{\mathbf{P}}_k}}{\left\|\overrightarrow{\mathbf{O}\widehat{\mathbf{P}}_k}\right\|} \tag{7}$$

is the unit vector approximating the object orientation in the 3D space. The vector $\mathbf{j}'_k$ is the vector $\mathbf{j} = (0,1,0)$ rotated by the unknowns $\widehat{\varphi}_k, \widehat{\delta}_k$ and $\widehat{\gamma}_k$ around $\mathbf{x}, \mathbf{z}'$ and $\mathbf{y}''$:

$$\mathbf{j}'_k = \mathbf{R}_{\mathbf{y}''}(\widehat{\gamma}_k)\mathbf{R}_{\mathbf{z}'}(\widehat{\delta}_k)\mathbf{R}_{\mathbf{x}}(\widehat{\varphi}_k)\mathbf{j}, \tag{8}$$

where $\mathbf{z}'$ is the axis $\mathbf{z}$ rotated around $\mathbf{x}$ by φ, and $\mathbf{y}''$ is $\mathbf{y}$ rotated by first

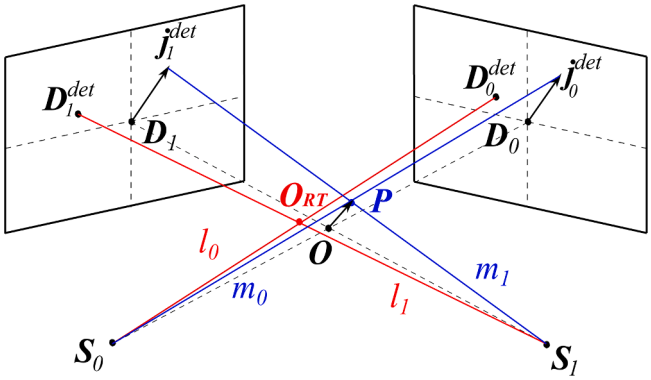

Fig. 4. Combination of two radiographs to recover the 3D pose.

Fig. 5. The CAD model of a chess bishop.

φ around $\mathbf{x}$ and then δ around $\mathbf{z}'$. For the sake of simplicity, we will express Eq. (8) in terms of *extrinsic* rotations, i.e. defined with respect to a fixed coordinate system, rather than *intrinsic* rotations, where the axis are updated after each rotation. In fact, any composition of intrinsic rotations can be expressed in terms of extrinsic rotations, by inverting the rotations' order. This means that, for the specific case in Eq. (8):

$$\mathbf{R} = \mathbf{R}_{\mathbf{y}''}(\gamma)\mathbf{R}_{\mathbf{z}'}(\delta)\mathbf{R}_{\mathbf{x}}(\varphi) = \mathbf{R}_{\mathbf{x}}(\varphi)\mathbf{R}_{\mathbf{z}}(\delta)\mathbf{R}_{\mathbf{y}}(\gamma). \tag{9}$$

A demonstration of this statement is reported in A. By substituting Eq. 9 into Eq. 8, and after matrices multiplication, $\mathbf{j}'_k$ is expressed as:

$$\mathbf{j}'_k = \begin{pmatrix} -\sin\widehat{\delta}_k \\ \cos\widehat{\varphi}_k\cos\widehat{\delta}_k \\ \sin\widehat{\varphi}_k\cos\widehat{\delta}_k \end{pmatrix}. \tag{10}$$

Consequently, we calculate $\widehat{\delta}_k = \arcsin(-\mathbf{j}'_k(1))$ and $\widehat{\varphi}_k = \arctan\left(\frac{\mathbf{j}'_k(3)}{\mathbf{j}'_k(2)}\right)$.

6. If $k > 0, \widehat{\gamma}^{loc}_k$ is refined with a lookup through the k-th extended library, based on the SSIM. To restrict the search, only the library images corresponding to $\widehat{\delta}_k$ and $\widehat{\varphi}_k$ are considered, rounded to the library discretization step.
7. If $k = K$, the acquisition process ends, otherwise $k := k + 1$.
8. In order to acquire a radiograph close to the successive visibility angle, the acquisition system is rotated by $\widehat{\gamma}^k_{rot} = \gamma^k_{vis} - \widehat{\gamma}^{k-1}_{loc}$, and the system geometry is updated: the coordinates of the source $\mathbf{S}_k$, detector center $\mathbf{D}_k$ and the unit vectors $\mathbf{u}_k$ and $\mathbf{v}_k$ are calculated by rotating $\mathbf{S}_{k-1}, \mathbf{D}_{k-1}, \mathbf{u}_{k-1}$ and $\mathbf{v}_{k-1}$ around the rotation axis by $\widehat{\gamma}^k_{rot}$. The procedure continues from step 1.

With the described procedure, the system is driven to acquire projections at the visibility angles based only on the estimate of the local orientation γ_{loc} of the object. However, the complete estimation of the

Table 1
The geometry and parameters of our experiments. The pixel size and resolution of the experiment on real data is after the 4×4 rebinning operation of the projections.

Exp	SOD	SDD	Proj size	ROI size	Pix size	Resol.
3.1.1	489.53 mm	764.88 mm	350×350	150×170	150 μm	98 μm
		Ω		**Discr.**	**γ-library**	
		$\{60°, 120°, 180°, 240°\}$		$0.1°$	$\gamma \in [0, 359.9]°$	
		Pose Perturb			**Ext libraries**	
		$\delta, \varphi \in [-2, 2]°, \gamma \in [0, 360)°$, $t_x, t_y, t_z \in [-3.5, 3.5]$ mm			$\varphi, \delta \in [-3.5, 3.5]°$, $\gamma \in [\gamma^k_{vis} - 2°, \gamma^k_{vis} + 2°]$	
Exp	**SOD**	**SDD**	**Proj size**	**ROI size**	**Pix size**	**Resol.**
3.1.2	489.53 mm	764.88 mm	766×970	321×111	150 μm	98 μm
		Ω		**Discr.**	**γ-library**	
		$\{0°, 222.5°, 85°, 307.5°, \ldots\}$		$0.1°$	$\gamma \in [0, 359.9]°$	
		Pose Perturb			**Ext libraries**	
		$\delta, \varphi \in [-2, 2]°, \gamma \in [0, 360)°$, $t_x, t_y, t_z \in [-3.5, 3.5]$ mm			–	
Exp	**SOD**	**SDD**	**Proj size**	**ROI size**	**Pix size**	**Resol.**
3.1.3	489.53 mm	764.88 mm	766×970	321×111	150 μm	98 μm
		Ω		**Discr.**	**γ-library**	
		$\{0°, 86.2°, 192.4°\}$		$0.1°$	$\gamma \in [0, 89.9]°$	
		Pose Perturb			**Ext libraries**	
		$\delta, \varphi \in [-3, 3]°, \gamma \in [0, 90)°$, $t_x, t_y, t_z \in [-3, 3]$ mm			$\varphi, \delta \in [-3.5, 3.5]°$, $\gamma \in [\gamma^k_{vis} - 1.8°, \gamma^k_{vis} + 1.8°]$	
Exp	**SOD**	**SDD**	**Proj size**	**ROI size**	**Pix size**	**Resol.**
3.2	125.00 mm	750.00 mm	2656×1056	321×111	600 μm	100 μm
		Ω		**Discr.**	**γ-library**	
		$\{0°, 86.2°, 192.4°\}$		$0.1°$	$\gamma \in [0, 89.9]°$	
		Pose Perturb			**Ext libraries**	
		–			$\varphi, \delta \in [-3.5, 3.5]°$, $\gamma \in [\gamma^k_{vis} - 1.8°, \gamma^k_{vis} + 1.8°]$	

Fig. 6. The CAD model of the syringe used in our experiments.

pose of the object is an added value to our work and could be used in case a more flexible system would be available (for example with the source and detector placed on robotic arms). In this case, the preferred orientations to be acquired could be defined in 3D based with 6 degrees of freedom, and the robotic arms could be driven towards the acquisition of these views.

3. Experiments

In this section, we describe experiments that were run to validate our method with simulated as well as with real data.

3.1. Simulated data experiments

To test the accuracy of DynaPose on estimating the object pose and consequently acquiring the visibility angles, we first conducted 20 experiments on a simple CAD model of a chess bishop in Section 3.1.1. To evaluate the convergence of the estimates to the ground truth parameters, in Section 3.1.2 20 experiments were conducted on an assembly of a syringe, with 20 golden ratio distributed visibility angles to be acquired. In Section 3.1.3, the robustness of the method to noise was investigated by performing experiments on the syringe model to acquire 3 visibility angles. In particular, 20 experiments were run both on noiseless data and on noisy data with 4 levels of noise. For the experiments on noisy data, the average over 5 realizations was reported.

3.1.1. Noiseless data experiment on a single CAD model

To evaluate the accuracy of the pose estimation and the dynamic acquisition in the vicinity of the visibility angles, noiseless simulation experiments were run with a CAD model of a chess bishop (see Fig. 5) with a bounding box of size $[12.50 \times 27.86 \times 12.50]$ mm. Radiographs were simulated from the CAD model with the system parameters presented in Table 1. A set of twenty experiments was run by randomly initiating the pose of the object, by varying $\delta, \varphi \in [-2, 2]^\circ, \gamma \in [0, 360)^\circ$ and $t_x, t_y, t_z \in [-3.5, 3.5]$ mm. A γ-library of 150×170 ROI projection images was created with $(t_x, t_y, t_z) = (0, 0, 0)mm, \delta = 0^\circ, \varphi = 0^\circ$, and by varying $\gamma \in \{0, 0.1, \ldots, 359.9\}^\circ$. For these experiments, the visibility angles are chosen as: $\Omega = \{\gamma_{vis}^1, \gamma_{vis}^2, \gamma_{vis}^3, \gamma_{vis}^4\} = \{60^\circ, 120^\circ, 180^\circ, 240^\circ\}$. Extended libraries were created in the neighborhood of the visibility angles by varying $\varphi, \delta \in [-3, 3]^\circ$ and $\gamma \in [\gamma_{vis}^k - 2^\circ, \gamma_{vis}^k + 2^\circ]$, with discrete steps of 0.1°.

3.1.2. Noiseless data experiment on an assembly

We conducted experiments on an assembly of a syringe with 90° axial symmetry, composed of 9 components. In Fig. 6, the CAD model of the sample is shown. The syringe is mainly composed of plastic and metal: five of the components (the main body, the needle cover and guide) are made of propylene, one component is made of polycarbonate, one is made of MABS thermoplastic and two (the needle and spring) are made of steel. In simulation experiments, these metallic components are not projected, as their registration was challenging. The spectrum of the source was estimated using real data measurements, as explained in Section 2.2. The system parameters for these simulations are listed in Table 1. The dimensions of the CAD model after assembly of the components, were $[15.58 \times 62.60 \times 15.58]$ mm. Twenty experiments were run by randomly initiating the object pose, with $\gamma \in [0, 90)^\circ, \delta, \varphi \in [-3, 3]^\circ$ and $t_x, t_y, t_z \in [-3, 3]$ mm. Due to the symmetry of the CAD model, the γ-library for 2D registration was created by varying $\gamma \in [0, 89.9]^\circ$, with an angular step of 0.1°.

To test the accuracy limit of DynaPose, $K = 20$ visibility angles were determined with a golden ratio distribution (Kaestner, Munch, & Trtik, 2011). For practical reasons, extended libraries were not generated and steps (3b) and (6) were skipped. The orientation γ_{loc}^k was retrieved with step (3a), for all $k = 0, \ldots, 20$.

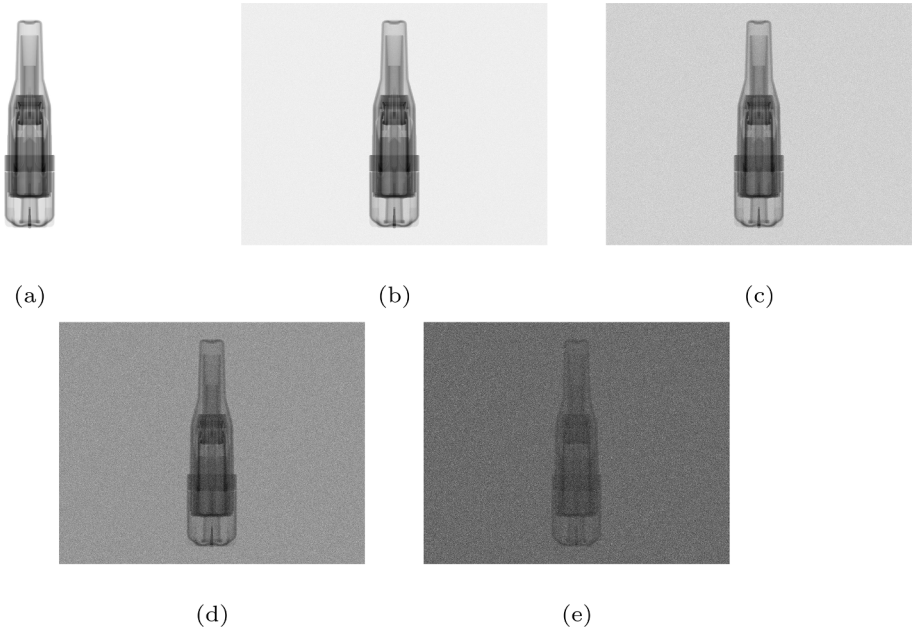

Fig. 7. Noiseless simulated projection of a syringe (a) and noisy simulated projections with increasing levels of Poisson noise ($I_0 = 10^5, 10^4, 10^3, 10^2$ in (b), (c), (d) and (e), respectively).

3.1.3. Noisy data experiment on an assembly

To study the performance of our method with respect to noise, the experiment of Section 3.1.2 was repeated for various levels of noise and a limited set of visibility angles. Based on the γ-library, three visibility angles, $\Omega = \{\gamma_{vis}^1, \gamma_{vis}^2, \gamma_{vis}^3\} = \{0^\circ, 86.2^\circ, 172.4^\circ\}$, were identified by considering the visibility contrast of a specific component, as defined in Section 2.3. In order to improve the estimate of γ by optimizing for the other two angles, extended libraries around the visibility angles were built. To do so, by comparing between the γ-library and noiseless simulated images with $\varphi, \delta \in [-3, 3]^\circ$ and $\gamma \in [0, 89.9]^\circ$, discretized by step of 0.1°, we quantified the maximum absolute error on the estimate of γ as $\epsilon = 1.8^\circ$. Then, extended libraries were created around the visibility angles γ_{vis}^k, $k = 1, \ldots, 3$, by varying $\varphi, \delta \in [-3.5, 3.5]^\circ$ and $\gamma \in [\gamma_{vis}^k - \epsilon, \gamma_{vis}^k + \epsilon]$, with an angular step of 0.1°.

To test the robustness of DynaPose to noise, increasing levels of noise were considered. Poisson noise was added to the simulated radiographs, with beam intensity $I_0 = 10^2, 10^3, 10^4, 10^5$. To quantify the amount of generated noise, we calculated the signal-to-noise ratio (SNR), on a 50×50 ROI in the background, as:

$$SNR = 10\log_{10}\left(\frac{\mu}{\sigma}\right), \tag{11}$$

where μ is the average intensity of the ROI, and σ is its standard deviation. The average SNR in our simulated projections was 7.8, 12.8, 17.8 and 22.8 dB, corresponding to $I_0 = 10^2, 10^3, 10^4$ and 10^5, respectively (see Fig. 7).

In order to compare DynaPose to a conventional registration method, the CAD model in its default pose was aligned to the CAD model with a perturbed pose by using an iterative closest point (ICP) algorithm. The pose parameters were finally obtained from the resulting transformation matrix. Finally, measured projection images at the visibility angles were compared to simulated projections from (i) the extended libraries, (ii) the CAD model using the parameters obtained with DynaPose and (iii) the CAD model using the parameters obtained with the ICP alignment.

3.2. Real data experiment on an assembly

DynaPose was also evaluated with real data of a syringe of which the CAD model was used in the previous experiments. The syringe was imaged with a TESCAN UniTOM XL equipped with an open directional tube with a 2 µm spot size and a Perkin Elmer flat panel detector with a square pixel size of 0.15 mm. A set of 3600 2656 × 1056 equiangular radiographs spanning 360° was acquired at 80 kVp, with the geometry shown in Table 1. The spectrum of the source was optimized as in Section 2.2. As the needle and spring are allowed to move with a certain degree of freedom inside the syringe, and as the spring can deform, these components were not projected in the simulated data. In real data, they were segmented out by thresholding the projections based on intensity values, and the same areas were segmented out in simulated data as not to influence image registration. Due to the complexity of this sample, where each component is allowed to move independently from each other, the real data experiment appears to be challenging, as the 2D/3D registration method needs to be robust to small deviations and misalignments. In order to reduce the memory requirements of the libraries, the simulated projections of the ROIs for alignment were rebinned to (4×4) bin size, resulting in a 0.6 mm detector pixel size. The ROIs were then composed of 321×111 pixels, with a resolution of 0.1 mm. For this experiment, extended libraries were built for the same visibility angles and with the same extent of the parameters as in Section 3.1.3.

In order to compare DynaPose to a conventional 3D registration approach, 2D slices were reconstructed from the measured projections with the Feldkamp, Davis and Kress (FDK) algorithm (Feldkamp, Davis, & Kress, 1984). The reconstructed volume was then post-processed in Dragonfly (Object Research Systems (ORS)), to extract a triangular mesh. The components of the assembly were merged together and aligned to the reconstructed STL by using an ICP algorithm. The pose parameters were finally obtained from the resulting transformation

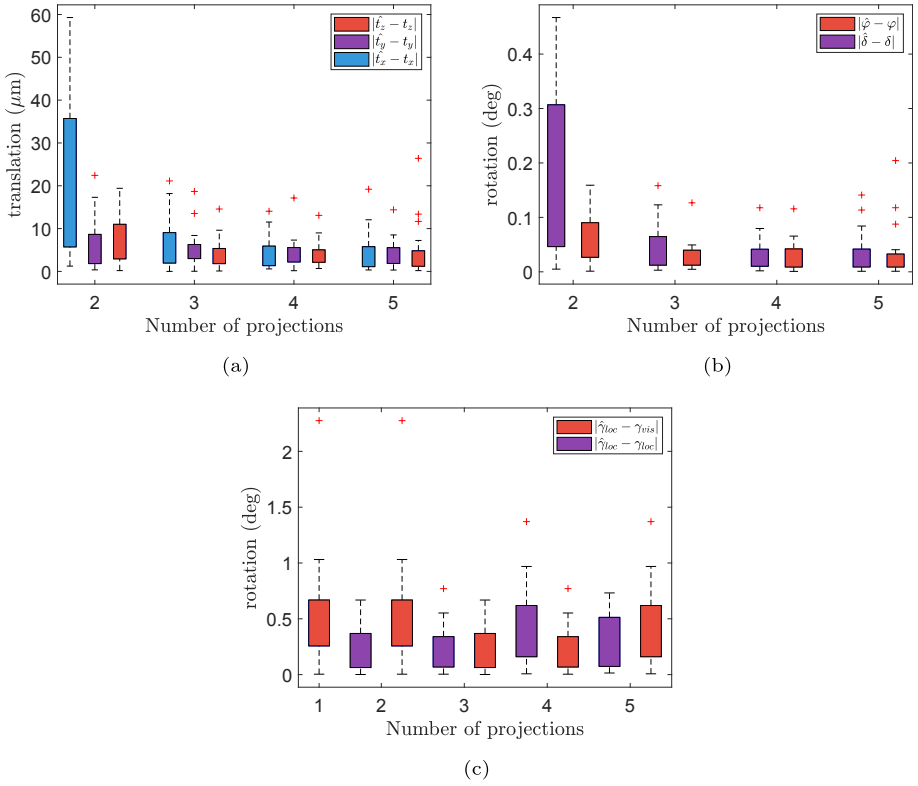

Fig. 8. Estimate of the translation (a), and rotations (b,c) of the chess bishop based on noiseless simulated projections. Figure (c) reports the absolute error between the estimated local γ and both its ground truth value (purple) and the visibility angle value (red).

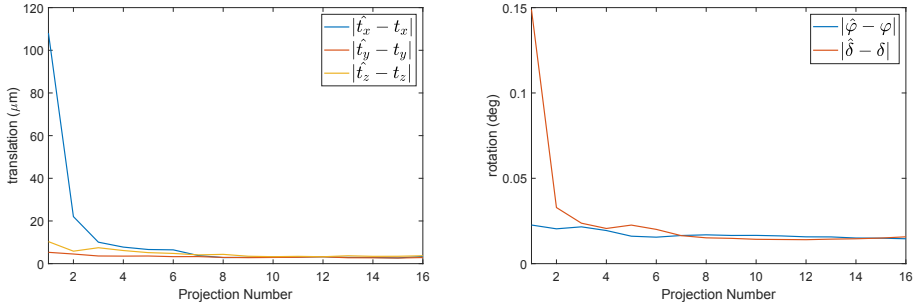

(a) (b)

Fig. 9. Evaluation of the convergence of the position (a) and rotation (b) estimates from simulated radiographs of a syringe, for 20 golden ratio distributed visibility angles.

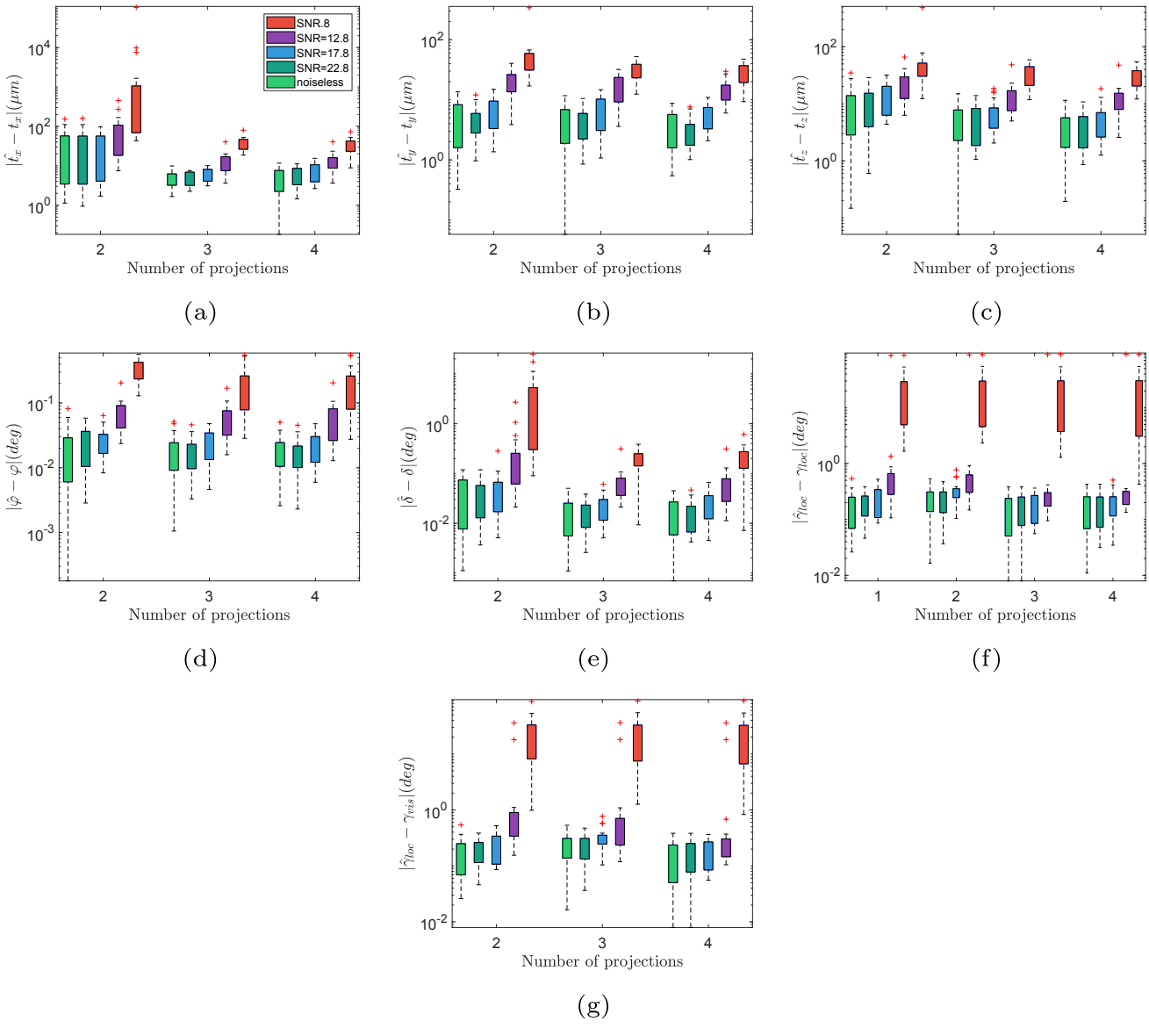

(a) (b) (c) (d) (e) (f) (g)

Fig. 10. 3D orientation estimate of a CAD-based syringe for different SNR based on simulated projections.

Table 2
Mean and standard deviations of the absolute error between the ground truth pose parameters and their estimates at different levels of noise.

		1 proj		2 proj		3 proj		4 proj	
	SNR [dB]	mean	STD	mean	STD	mean	STD	mean	STD
t_x (μm)	∞			37	45	5	2	5	3
	22.8			35	44	5	2	6	3
	17.8			34	35	6	2	7	4
	12.8			83	110	13	8	13	8
	7.8			6379	23402	38	15	33	15
t_y (μm)	∞			5	4	4	3	4	3
	22.8			5	3	4	2	3	2
	17.8			7	4	7	4	6	3
	12.8			20	10	16	8	14	6
	7.8			57	69	32	11	26	10
t_z (μm)	∞			10	10	5	4	4	3
	22.8			10	9	5	4	4	3
	17.8			13	9	7	5	6	4
	12.8			23	15	14	10	13	9
	7.8			63	100	33	14	30	11
$\varphi(deg)$	∞			0.02	0.02	0.02	0.01	0.02	0.01
	22.8			0.02	0.02	0.02	0.01	0.02	0.01
	17.8			0.03	0.01	0.02	0.01	0.02	0.01
	12.8			0.07	0.04	0.06	0.04	0.06	0.04
	7.8			0.33	0.14	0.20	0.15	0.20	0.15
$\delta(deg)$	∞			0.04	0.04	0.02	0.01	0.02	0.01
	22.8			0.04	0.03	0.02	0.01	0.02	0.01
	17.8			0.05	0.06	0.02	0.02	0.03	0.02
	12.8			0.32	0.62	0.07	0.06	0.07	0.07
	7.8			4.04	7.08	0.19	0.09	0.21	0.13
$\gamma(deg)$	∞	0.18	0.13	0.23	0.15	0.15	0.11	0.18	0.13
	22.8	0.19	0.10	0.24	0.11	0.16	0.11	0.18	0.12
	17.8	0.24	0.14	0.32	0.16	0.18	0.10	0.20	0.12
	12.8	4.78	19.21	4.85	19.61	4.69	19.90	4.76	20.19
	7.8	21.20	22.17	21.38	22.60	20.86	22.91	20.60	23.20

matrix. Finally, measured projection images at the visibility angles were compared to simulated projections from (i) the extended libraries, (ii) the CAD model using the parameters obtained with DynaPose and (iii) the CAD model using the parameters obtained with the ICP alignment.

4. Results and discussion

4.1. Simulated data experiment

The accuracy of our methodology for the chess bishop is shown in Fig. 8. The absolute difference with the ground truth parameters is shown, as a function of the number of acquired projections. For γ, to validate the accuracy of the pose estimation, the distance between the estimated value and the ground truth local value is reported. Moreover, to demonstrate the efficacy of DynaPose on the acquisition close to the visibility angles, the distance to the visibility angle is shown. Note that this last value cannot be calculated at the first projection.

Table 3
The mean of the SSIM and FSIM between the ground truth projections and library images after alignment.

	SNR [dB]	1 proj	2 proj	3 proj	4 proj
SSIM	∞	0.9708	0.9684	0.9708	0.9707
	22.8	0.6878	0.6946	0.6778	0.6869
	17.8	0.5671	0.5781	0.5669	0.5707
	12.8	0.3671	0.3732	0.3681	0.3634
	7.8	0.2406	0.2305	0.2412	0.2319
FSIM	∞	0.9970	0.9972	0.9978	0.9976
	22.8	0.9936	0.9926	0.9932	0.9928
	17.8	0.9661	0.9598	0.9609	0.9594
	12.8	0.8443	0.8251	0.8214	0.8192
	7.8	0.6642	0.6230	0.6274	0.6192

The results of the noiseless data experiment on an assembly described in Section 3.1.2 are shown in Fig. 9. The improvement of the estimates is reported in function of the number of acquired projections. The plot shows that the error on the translation estimates stabilizes between 2.5 and 3 μm after the first 8 visibility angles. The same amount of acquisitions is sufficient for the error on the orientation estimates to be below 0.015°. These findings demonstrate that, for noiseless simulated data, DynaPose can obtain subpixel accuracy on the pose estimation by using very few projections.

The accuracy of DynaPose in function of the noise level, as described in 3.1.3, is shown in Fig. 10 and Table 2. For every noise level, the mean over 5 realizations is reported. Except for the highest noise level, after 4 projections the position error is, on average, below 14 μm, which is well below the effective pixel size. A similar result can be observed for the rotation angles δ and φ, which are estimated up to tenths to hundredths of degrees. For γ, a substantial decrease in accuracy can be observed from SNR = 12.8 dB. As the error does not improve with the extended libraries comparison, we believe that, for this or higher noise levels, the angular range $\in$ of the extended libraries should be increased and calculated directly on noisy simulated projections.

By observing the results of experiments on synthetic data, one may notice that, at the first estimate, $\widehat{t}_x$ and $\widehat{\delta}$ are less accurate than the other parameters. A possible explanation for this might be that the latter are parallel to the detector plane at the first acquisition, hence, in theory, they could be estimated from only one projection. To estimate $\widehat{t}_x$ and $\widehat{\delta}$, instead, more 3D information is needed. The errors in Table 2 suggest the same conclusion: in presence of noise, the estimates of these parameters reach the same accuracy as the others only by exploiting three projections or more.

As can be seen from the comparison of noiseless experiments in Fig. 8

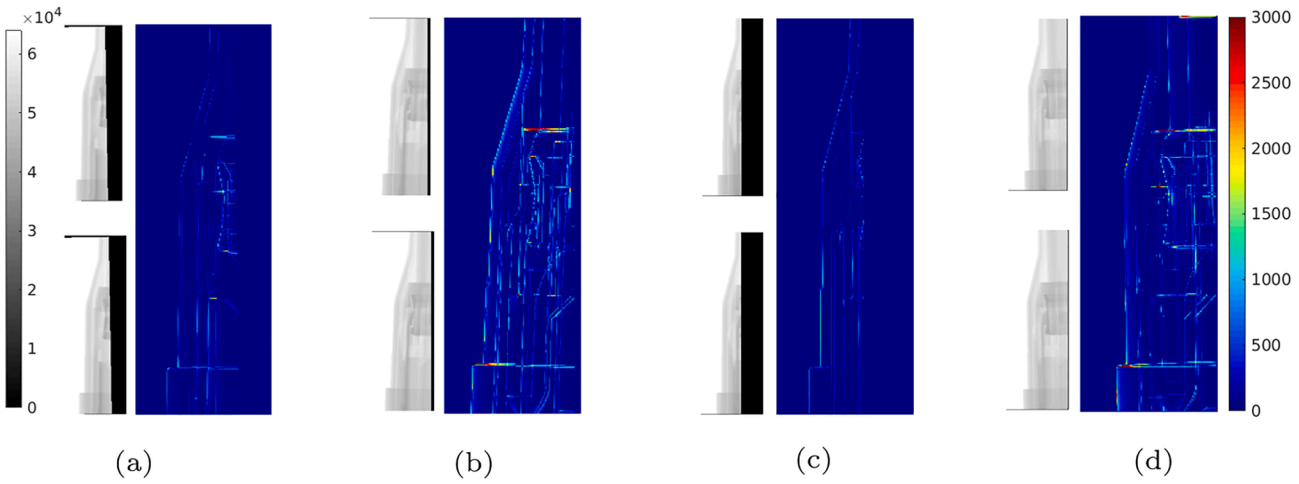

Fig. 11. Comparison of noiseless ground truth and simulated library projections after alignment, at the first acquired projection angle and those selected with DynaPose. In the upper grayscale image the ground truth image is shown, in the lower grayscale image the simulated image is shown, and in the colored image the difference between simulated and measured data is shown.

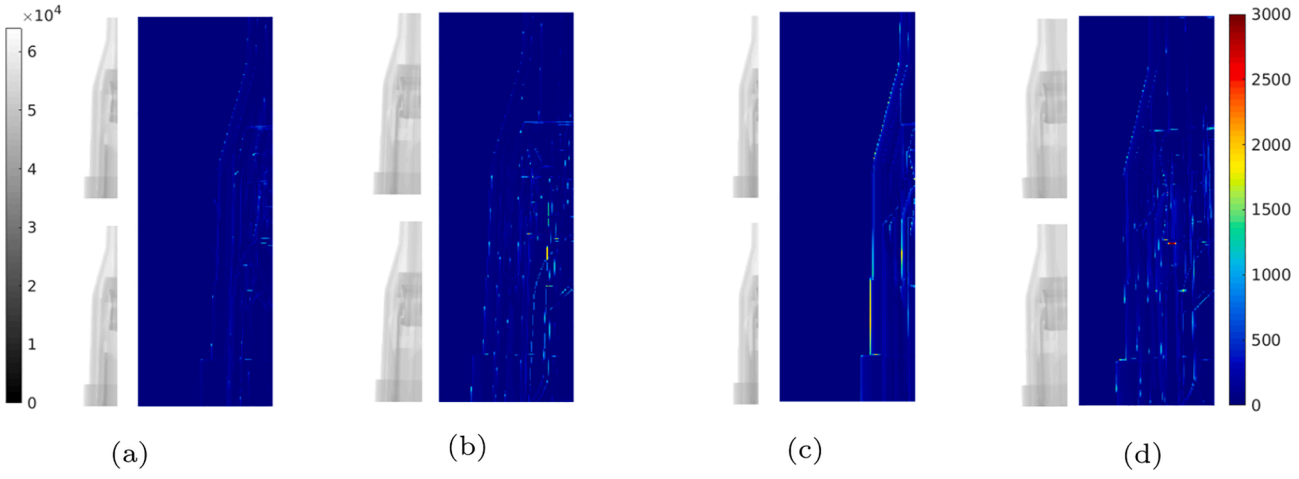

Fig. 12. Comparison of noiseless ground truth and simulated projections with the parameters estimated with DynaPose, at the first acquired projection angle and those selected with DynaPose. In the upper grayscale image the ground truth image is shown, in the lower grayscale image the simulated image is shown, and in the colored image the difference between simulated and measured data is shown.

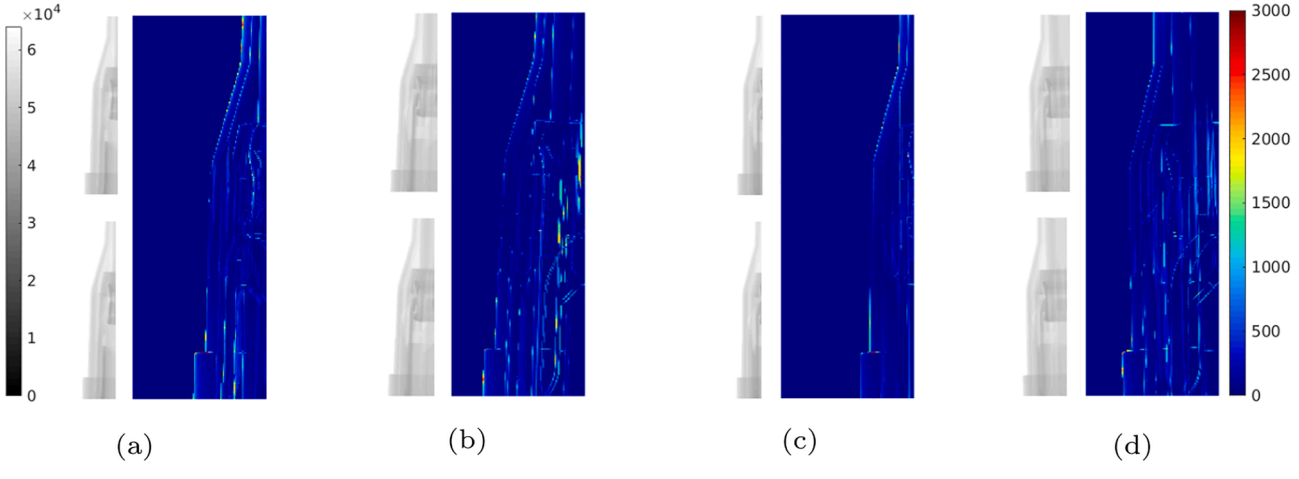

Fig. 13. Comparison of noiseless ground truth and simulated projections with the parameters estimated with the ICP algorithm, at the first acquired projection angle and those selected with DynaPose. In the upper grayscale image the ground truth image is shown, in the lower grayscale image the simulated image is shown, and in the colored image the difference between simulated and measured data is shown.

Table 4
Mean squared error between the measured projections and library simulated projections after alignment, projections simulated with the object parameters estimated with DynaPose and with the ICP alignment.

Projection	MSE Library	MSE DynaPose	MSE ICP
1	1.4×10^6	1.2×10^6	1.3×10^6
2	1.1×10^6	8.1×10^5	9.2×10^5
3	1.3×10^6	1.2×10^6	1.2×10^6
4	8.7×10^5	8.1×10^5	9.2×10^5

with those in Fig. 10, the latter achieve an accuracy of 0.1° on the γ estimate, that is the discretization step of the library. This is not the case for the experiment on the chess bishop, although the detector resolution and the library discretization are the same. This result may be explained by the fact that the chess bishop and the ROI for alignment are both relatively small compared to those of the syringe, so that the features used for comparison are also smaller. Moreover, the complexity of the syringe, in this case, plays in our favour, as it provides more elements of comparison between the projections. The simplicity of the chess piece, instead, makes the alignment a harder task, as it reduces the comparison with the library images to a single, very small feature.

In general, the results on simulated data show a subpixel accuracy on the pose estimation with very few projections, even for high noise levels. Depending on the requirements of the inspection task, one can make a compromise between accuracy and speed.

To quantify the similarity between the ground truth projections and the library ones after alignment, similarity indexes between the images are presented in Table 3. Here, the mean SSIM and feature similarity index (FSIM) (Zhang, Zhang, Mou, & Zhang, 2011) over the realizations are reported, divided for projection number. As expected, the similarity indexes worsen as the noise level increases.

To visualize the accuracy of alignment of DynaPose, difference images between the noiseless ground truth projections and the library

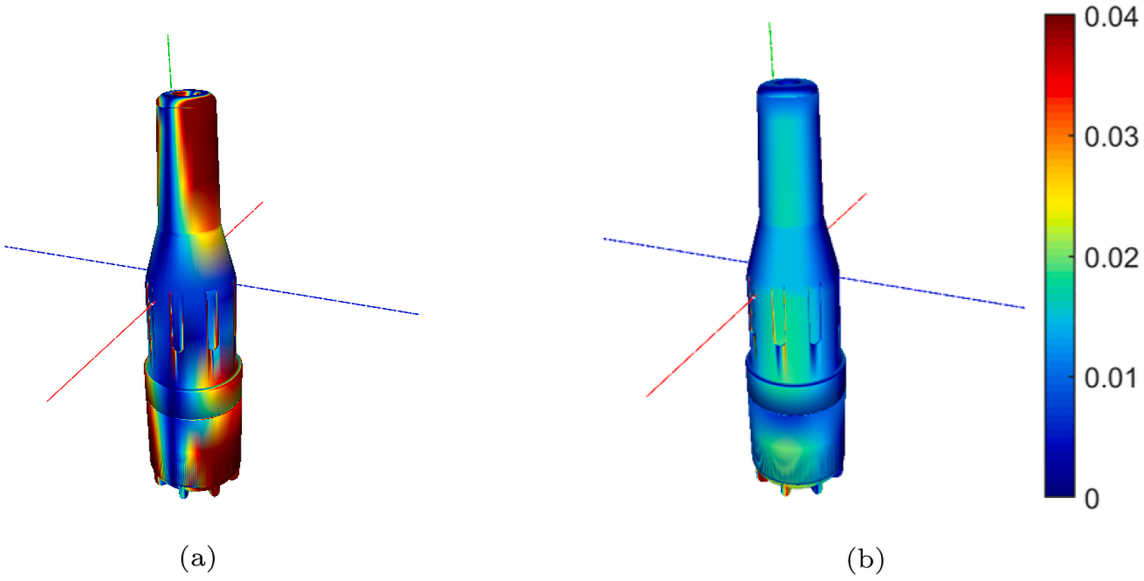

Fig. 14. A 3D comparison between the alignment achieved with ICP (a) and DynaPose (b) methods. The aligned CAD model is colored based on the Hausdorff distance in mm between its vertices and those of the model at perturbed pose.

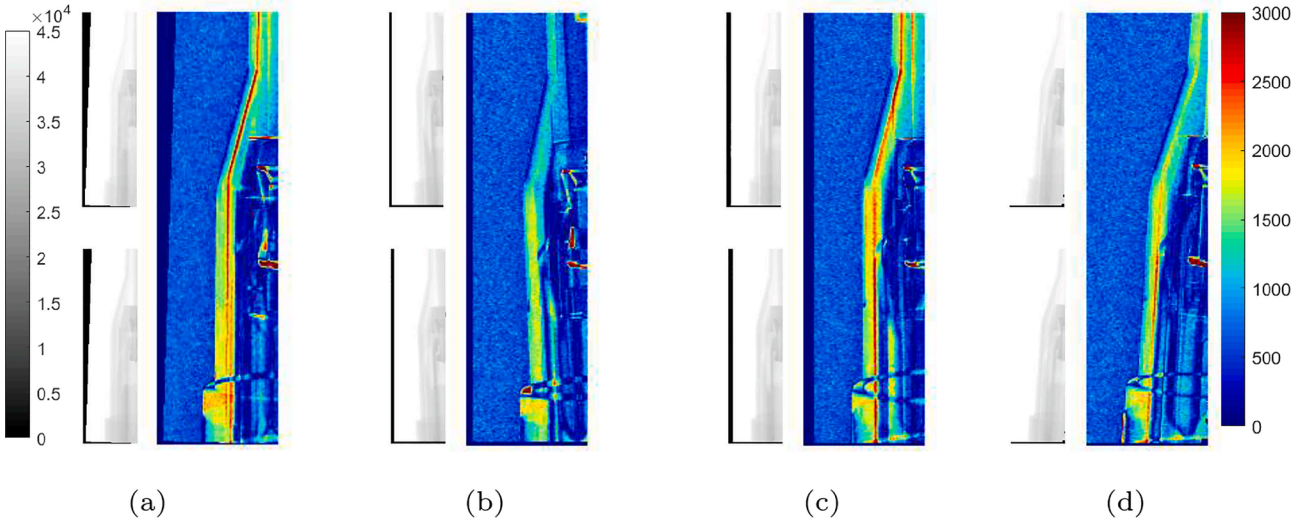

Fig. 15. Comparison of measured and simulated library projections after alignment, at the first acquired projection angle and those selected with DynaPose. In the upper grayscale image the measured image is shown, in the lower grayscale image the simulated image is shown, and in the colored image the difference between simulated and measured data is shown.

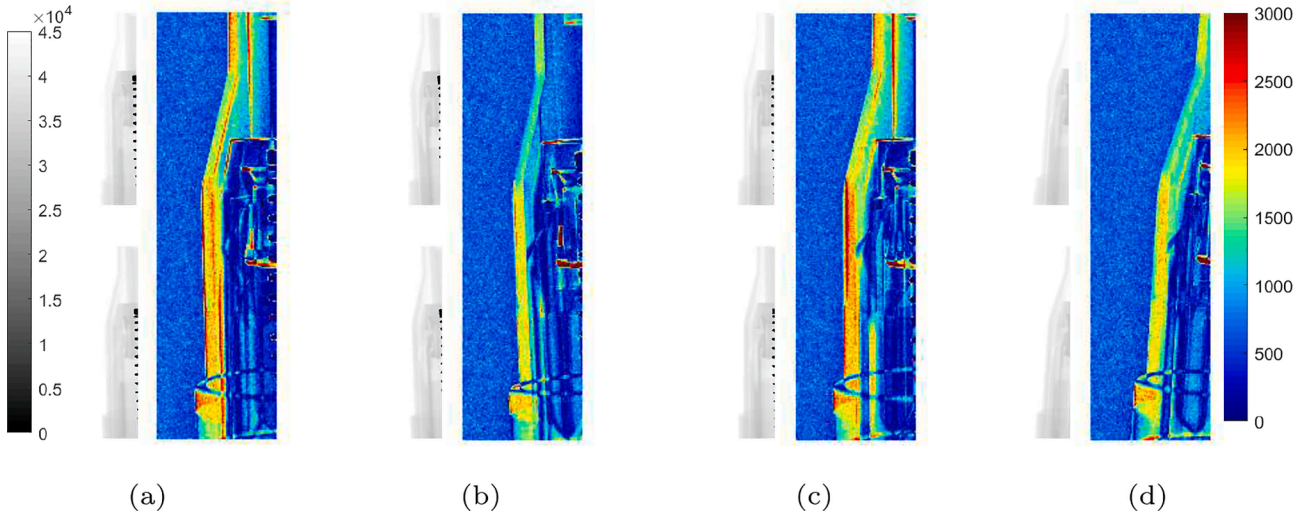

Fig. 16. Comparison of measured and simulated projections with the parameters estimated with DynaPose, at the first acquired projection angle and those selected with DynaPose. In the upper grayscale image the ground truth image is shown, in the lower grayscale image the simulated image is shown, and in the colored image the difference between simulated and measured data is shown.

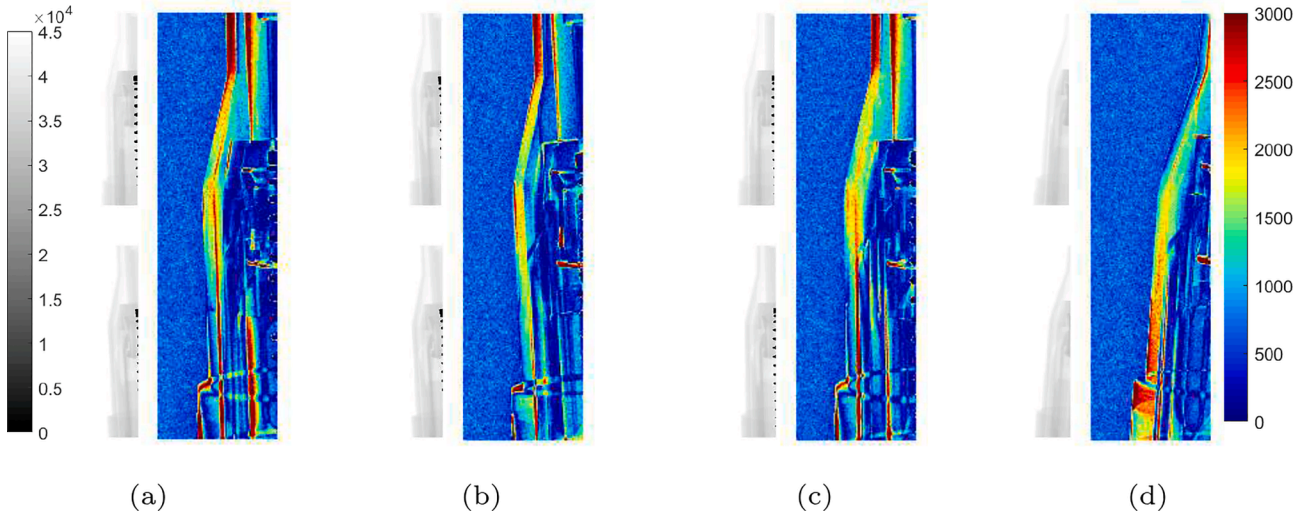

Fig. 17. Comparison of measured projections and simulated projections with the parameters estimated with the ICP algorithm, at the first acquired projection angle and those selected with DynaPose. In the upper grayscale image the measured image, in the lower grayscale image the simulated image, and in the colored one the difference between them.

projections after alignment are shown in Fig. 11. We also compared DynaPose to conventional state of the art methods on noiseless simulated data. Fig. 12 shows the difference images between ground truth projections and simulated projections from the CAD model with parameters estimated with DynaPose, while Fig. 13, shows the difference images with the simulated projections with parameters estimated with the ICP algorithm. A quantitative comparison between the alignment methods are reported in Table 4. For a 3D comparison between the two alignments, the Hausdorff distance between the CAD model after alignment and the one at the perturbed pose is shown in Fig. 14. As can be seen from this comparison, DynaPose produces a better result.

4.2. Real data experiment

For the real data experiments, there were no ground truth parameters available to directly compare our estimates with. For this reason, we present difference images between the library simulated projections and aligned (rebinned) measured data in Fig. 15. Visual inspection clearly shows good agreement between the measured data and the CAD model projections. The difference maps do, however, show higher differences in the intensity of certain components. This may be due to an imprecise density assigned to the material. In future work, we intend to estimate the material density offline together with the source spectrum and system geometry parameters. Other discrepancies are present at all the projection angles. These are likely caused by a physical difference or misalignment between the CAD model components and the manufactured object. The results should, therefore, be interpreted by considering the complexity of the investigated object: every component of the assembly is independent and can, to a degree, move autonomously with respect to the other components. These results demonstrate the robustness of our 2D/3D alignment procedure in presence of outliers.

We also compared DynaPose to conventional 3D registration. Fig. 16 shows the difference images between measured projections and simulated projections from the CAD model with parameters estimated with DynaPose. Fig. 17 shows, instead, difference images between measured projections and simulated projections with orientation parameters estimated with the ICP algorithm, at the same projection angles as for the previous visualizations. To quantify the deviation, in Table 2 the

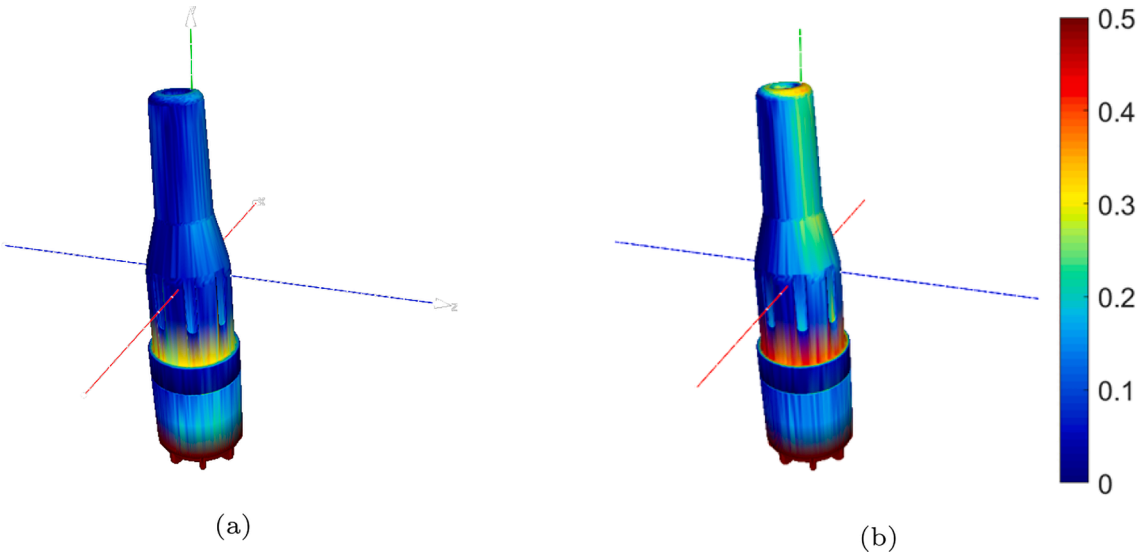

Fig. 18. A 3D comparison between the alignment achieved with ICP (a) and DynaPose (b) methods. The aligned CAD model is colored based on the Hausdorff distance in mm between its vertices and those of the reconstructed STL from measured data.

mean squared error between the images in Figs. 15–17 is reported. These quantities confirm the visual results: by using our method, a better fit to the measured data is achieved. Moreover, the MSE between measured images and simulated images with the object parameters estimated with DynaPose is always lower than the one between measured projections and library images. This was expected, since the library images are generated at discretized angles, and the alignment accuracy depends on the discretization step. In Fig. 18, a volumetric comparison between the ICP alignment and the alignment achieved with the DynaPose method, based on the Hausdorff distance between he meshes. Overall, an excellent agreement was found between the projected CAD data and the measurements, comparable to the results obtained with conventional reconstruction and 3D registration. Since DynaPose is a few-view method and does not require reconstruction, it opens up a pathway towards fast projection-based 3D inspection.

4.3. Computational time

The objects considered in our experiments are approximately axially symmetric. This way, at iteration 2 of Section 2.5, the measured projection needs to be aligned with only one of the images in the γ-libraries since, due to the symmetry, it will be automatically aligned with all the library images. Taking this into account, the DynaPose method applied to the experiment in Section 4.2 takes 44.4 s in matlab on a single 2.1Ghz Intel Xeon E5-2610 CPU. The 2D registration and image warping takes 2.20 s. In case a non-symmetric object is considered, the object would look differently at every orientation. In this case, the measured projection needs to be registered to each projection image, thus increasing the total computational time by (2.20 s) $\times$ (nr. projections in the γ library) $\times$ (nr. acquisitions). This leads to a computational time higher than 2 h. However, with a GPU implementation and parallelization of operations, the performance should be comparable to the one observed in our experiments.

Compared to other methods, Dynapose not only reduces acquisition time by drastically decreasing the amount of acquisitions, but also has a great advantage avoiding 3D reconstruction. Standard CT methods that deal with very few acquisitions, need in fact to sum up the volume reconstruction and registration cost, the expensive post-processing to remove artifacts from the reconstruction (see, for example, Purisha et al., 2018, where the statistical reconstruction requires more than 2 h).

5. Conclusion

In this paper, DynaPose was introduced, a few-view method that enables 3D X-ray inspection of objects generated from a CAD model using a limited set of radiographs that are dynamically acquired during scanning. An efficient framework was introduced to determine and acquire the most informative view angles for a given CAD-based object and a given task. DynaPose was tested both on simulated and real data, and it was shown that, for the example experiments, subpixel accuracy could be achieved. The DynaPose dynamic inspection strategy can easily be adapted to different tasks, systems and samples with the pre-processing steps described in our paper.

A possible downside of our approach is the necessity to determine a region of interest (ROI) that is large enough to guarantee a successful registration. In our work, this ROI was manually selected. However, the definition of the ROI for a specific object and task is a one-time calculation. That is, once it is pre-computed, DynaPose can be executed smoothly on a large number of objects, for example in an inline setting. Further studies may be conducted to enable an automated optimal ROI selection for alignment and inspection. Another limitation is the computational cost of the proposed approach for the registration of non-symmetrical objects. In this case, the 2D image registration between the measured image and all the images of the library would be, in fact, necessary. To improve performance, a GPU implementation and parallelization could be considered. In future work, we intend to extend DynaPose to every kind of object shape, for example by using convolutional neural networks to predict the pose parameters directly from projection images.

Compared to conventional 3DCT inspection, DynaPose allows 3D inspection directly in the projection space, without the need for reconstruction. It applies to cases of both a limited number of projections and a limited angular view, and therefore opens a pathway towards fast industrial inspection of each individual product.

CRediT authorship contribution statement

Alice Presenti: Writing - original draft, Writing - review & editing, Methodology, Validation. **Jan Sijbers:** Writing - original draft, Writing - review & editing, Methodology, Validation. **Jan De Beenhouwer:** Writing - original draft, Writing - review & editing. Methodology, Validation

Declaration of Competing Interest

The authors declare that they have no known competing financial interests or personal relationships that could have appeared to influence the work reported in this paper.

Acknowledgment

This research is funded by the FWO SBO projects S004217N and S003421N, the FWO projects G094320N and G090020N, and the European Commission through the INTERREG Vlaanderen Nederland program project Smart*Light (0386). The authors would like to thank Tescan XRE NV for acquiring the radiographic images.

Appendix A

Any composition of intrinsic rotations can be expressed in terms of extrinsic ones, by inverting the order of the rotations. Let us give a demonstration for the case in Eq. 8, which extends to other orders of rotations. Rotating a vector around $\mathbf{z}'$ by δ is equivalent to first rotating it back around $\mathbf{x}$ by $-\varphi$, then rotating around $\mathbf{z}$ by δ and finally rotating around $\mathbf{x}$ by φ :

$$\mathbf{R}_{z'}(\delta) = \mathbf{R}_x(\varphi)\mathbf{R}_z(\delta)\mathbf{R}_x(\varphi)^{-1}. \tag{A.1}$$

Equivalently for $\mathbf{y}''$:

$$\mathbf{R}_{y''}(\gamma) = \mathbf{R}_{z'}(\delta)\mathbf{R}_{y'}(\gamma)\mathbf{R}_{z'}(\delta)^{-1}. \tag{A.2}$$

By substituting Eq. (A.1), in Eq. (8) we obtain:

$$\mathbf{R} = \mathbf{R}_{y''}(\gamma)\mathbf{R}_{z'}(\delta)\mathbf{R}_x(\varphi) = \mathbf{R}_x(\varphi)\mathbf{R}_z(\delta)\mathbf{R}_y(\gamma), \tag{A.3}$$

Q.E.D.

References

Boaretto, N., & Centeno, T. M. (2017). Automated detection of welding defects in pipelines from radiographic images DWDI. *NDT & E International, 86*, 7–13.

Brunke, O. (2012). Fully-Automated metrology and defect analysis with high-resolution 300 kV microfocus computed tomography. In *18th World Conference on Non Destructive Testing* (pp. 16–20).

Carrasco, M., & Mery, D. (2011). Automatic multiple view inspection using geometrical tracking and feature analysis in aluminum wheels. *Machine Vision and Applications, 22*, 157–170.

Eikenes, A. (2020). Intersection point of lines in 3D space. MATLAB Central File Exchange. Accessed: 11.05.2020.

Feldkamp, L. A., Davis, L. C., & Kress, J. W. (1984). Practical cone-beam algorithm. *Journal of the Optical Society of America A, 1*, 612–619.

Haario, H., Kallonen, A., Laine, M., Niemi, E., Purisha, Z., & Siltanen, S. (2016). Shape recovery from sparse tomographic X-ray data. arXiv preprint arXiv:1605.01285.

Hiller, J., & Hornberger, P. (2016). Measurement accuracy in X-ray computed tomography metrology: Toward a systematic analysis of interference effects in tomographic imaging. *Precision Engineering, 45*, 18–32.

Hou, W., Wei, Y., Guo, J., Jin, Y., & Zhu, C. (2018). Automatic detection of welding defects using deep neural network. *Journal of Physics: Conference Series, 933*, Article 012006.

Kaestner, A. P., Munch, B., & Trtik, P. (2011). Spatiotemporal computed tomography of dynamic processes. *Optical Engineering, 50*, 1–10.

Kiekens, K., Welkenhuyzen, F., Tan, Y., Bleys, P., Voet, A., Kruth, J. P., & Dewulf, W. (2011). A test object with parallel grooves for calibration and accuracy assessment of industrial computed tomography (CT) metrology. *Measurement Science and Technology, 22*, Article 115502.

Kruth, J. P., Beartscher, M., Carmignato, S., Schmitt, R., De Chiffre, L., & Weckmann, A. (2011). Computed tomography for dimensional metrology. *CIRP Annals-manufacturing Technology, 60*, 821–842.

Marinovszki, A., De Beenhouwer, J., & Sijbers, J. (2018). An efficient cad projector for X-ray projection based 3D inspection with the ASTRA toolbox. In *8th Conference on Industrial Computed Tomography*.

Mery, D. (2015). Inspection of complex objects using multiple-X-ray views. *IEEE/ASME Transactions on Mechatronics, 20*, 338–347.

Mery, D., & Arteta, C. (2017). Automatic defect recognition in X-ray testing using computer vision. In *2017 IEEE Winter Conference on Applications of Computer Vision (WACV)* (pp. 1026–1035).

Noble, A., Gupta, R., Mundy, J., Schmitz, A., Hartley, R., & Hoffman, W. (1995). CAD-based inspection using X-ray stereo. In Proceedings of 1995 IEEE International Conference on Robotics and Automation (pp. 2361–2366). volume 3.

Noel, J. (2008). Advantages of CT in 3D scanning of industrial parts. *3D Scanning Technologies Magazine, 1*(3), 18–23.

Object Research Systems (ORS) Inc, C., Montreal. Dragonfly 3.6 [computer software].

Purisha, Z., Jidling, C., Wahlström, N., Särkkä, S., & Schön, T.B. (2018). Probabilistic approach to limited-data computed tomography reconstruction. CoRR, abs/1809.03779.

Six, N., De Beenhouwer, J., & Sijbers, J. (2019). poly-DART: A discrete algebraic reconstruction technique for polychromatic X-ray CT. *Optics Express, 27*, 33670–33682.

Valavanis, I., & Kosmopoulos, D. (2010). Multiclass defect detection and classification in weld radiographic images using geometric and texture features. *Expert Systems with Applications, 37*, 7606–7614.

Yin, Z., Khare, K., & De Man, B. (2009). Parametric boundary reconstruction algorithm for industrial CT metrology application. *Journal of X-ray Science and Technology, 17*, 115–133.

Zapata, J., Vilar, R., & Ruiz, R. (2011). Performance evaluation of an automatic inspection system of weld defects in radiographic images based on neuro-classifiers. *Expert Systems with Applications, 38*, 8812–8824.

Zhang, H., Li, L., Qiao, K., Wang, L., Yan, B., Li, L., & Hu, G. (2016). Image prediction for limited-angle tomography via deep learning with convolutional neural network.

Zhang, L., Zhang, L., Mou, X., & Zhang, D. (2011). Fsim: A feature similarity index for image quality assessment. *IEEE Transactions on Image Processing, 20*, 2378–2386.